Nonlinear effects of particle shape angularity in sheared granular media

Emilien Azéma,[1,*] Nicolas Estrada,[2,†] and Farhang Radjaï[1,‡]
[1]*LMGC, Université Montpellier 2, CNRS, Place Eugène Bataillon, 34095 Montpellier cedex 05, France*
[2]*Departamento de Ingeniería Civil y Ambiental, Universidad de Los Andes, Bogotá, Colombia*
(Received 4 April 2012; revised manuscript received 6 August 2012; published 1 October 2012)

We analyze the effects of particle shape angularity on the macroscopic shear behavior and texture of granular packings simulated by means of the contact dynamics method. The particles are regular polygons with an increasing number of sides ranging from 3 (triangles) to 60. The packings are analyzed in the steady shear state in terms of their shear strength, packing fraction, connectivity, and fabric and force anisotropies, as functions of the angularity. An interesting finding is that the shear strength increases with angularity up to a maximum value and saturates as the particles become more angular (below six sides). In contrast, the packing fraction declines towards a constant value, so that the packings of more angular particles are looser but have higher shear strength. We show that the increase of the shear strength at low angularity is due to an increase of both contact and force anisotropies and the saturation of the shear strength for higher angularities is a consequence of a rapid falloff of the contact and normal force anisotropies compensated for by an increase of the tangential force anisotropy. This transition reflects clearly the rather special geometrical properties of these highly angular shapes, implying that the stability of the packing relies strongly on the side-side contacts and the mobilization of friction forces.

DOI: 10.1103/PhysRevE.86.041301 PACS number(s): 45.70.−n, 83.80.Fg, 61.43.−j

I. INTRODUCTION

Granular materials composed of particles of complex shape are common in nature and also in various fields of science and engineering. Some examples are angular-shaped particles of soils and rocks, elongated or platy particles of pharmaceutical products, and nonconvex particles of metallurgical and sintered powders. These shape characteristics strongly affect the rheology and texture of granular materials. This has been recently evidenced by a number of numerical and experimental studies carried out using angular particles [1–12] and by a number of investigations that have focused on other important characteristics such as elongation [13–20] or nonconvexity [21,22]. The existing research results suggest that the effect of shape parameters is often nonlinear and counterintuitive, as in the case of the unmonotonic relation between the elongation of the particles and the packing fraction [13,14,18].

Hence, in order to obtain a clear picture of the complex behavior exhibited by real granular materials, it is crucial to understand and quantify the effects of particle shape. However, this is not an easy task, which is why systematic studies on the subject are scarce. One of the underlying issues is that it is difficult to control particle shape in experiments. Moreover, introducing particle shape in numerical simulations with discrete element methods gives rise to various technical difficulties, both geometrical and computational. One example of these difficulties involves contact detection and force calculation between particles of arbitrary shape [7,10,23–26].

The aim of this work is to explore the influence of the degree of angularity of the particles on the mechanical behavior of sheared granular packings. We employ the contact dynamics method to simulate large two-dimensional packings of polydisperse regular polygonal particles. We construct different packings, each of them made up of particles with a given number of sides varying from 3 (triangles) to 60. We also simulate a packing of disks, which may be considered as polygons of an infinite number of sides. Hence the angularity, defined as the exterior angle of polygons, varies from 0 for disks to $2\pi/3$ for triangles.

The packings are analyzed in the steady state in terms of their shear strength, packing fraction, connectivity, and fabric and force anisotropies as functions of the angularity. A pending issue that we would like to address in this paper is whether the packing of disks has a singular behavior compared to the packings of polygons. This is the case if a discontinuous change (within our statistical precision) is observed for a packing property, e.g. the shear strength or packing fraction, between the packing of disks and the packing of polygons of 60 sides, which are least angular polygons in our simulations. In a similar vein, it is not obvious whether packings composed of particles of the lowest numbers of sides, i.e., triangles and squares, are special compared to those of larger numbers of sides whose behavior is expected to be described by the angularity parameter as a deviation from circular shape.

In the following we introduce in Sec. II the numerical approach, system characteristics, and loading parameters. In Sec. III we focus on the evolution of shear strength and packing fraction with angularity. The microstructure is analyzed in Sec. IV in terms of connectivity, and contact and force anisotropies. Section V presents concluding remarks and a summary of the most salient results.

II. MODEL DESCRIPTION

A. Numerical method

The simulations were carried out by means of the contact dynamics (CD) method, which is suitable for large assemblies of undeformable particles. This method emerged from a mathematical formulation of nonsmooth dynamics and the subsequent algorithmic developments by Moreau [27–32] and Jean *et al.* [33–38]. The fundamental difference between this method and the common discrete element method (DEM)

*emilien.azema@univ-montp2.fr
†n.estrada22@uniandes.edu.co
‡farhang.radjai@univ-montp2.fr

or molecular dynamics (MD) approach lies in the treatment of small length and time scales involved in the dynamics of granular media. In MD-type DEM, pioneered by Cundall, the particles are treated as rigid bodies but the contacts between particles are assumed to obey a viscoelastic or plastic behavior in which the local strain variables are defined from the relative particle positions or displacements [39–52]. The time-stepping schemes used for the numerical integration of the equations of motion imply thus a fine resolution of the small time and length scales involved in contact interactions.

In the CD method these small scales are neglected and their effects absorbed into *contact laws* together with a *nonsmooth* formulation of particle dynamics described at the scale of particle displacements rather than small elastic response times and displacements. The equations of motion are integrated by an implicit time-stepping scheme by taking into account the kinematic constraints resulting from frictional contact interactions. The implicit integration makes the method unconditionally stable. Moreover, since in this method the elastic contact deflections are not resolved, the time step can be larger than that in the MD method where the time step should be small enough to allow for smooth variations of the overlap at the contact points to ensure numerical stability. In CD an iterative algorithm is used to determine the contact forces and particle velocities simultaneously at all potential contacts. A detailed presentation of the CD method is given in the Appendix for point contact interactions.

The particle shape enters a CD resolution algorithm through the explicit determination of the set of effective contacts at the beginning of a time step. For polygonal particles, two different types of contact can be distinguished: (i) side-vertex and (ii) side-side (see Fig. 1). A side-vertex contact is a point contact like that between two disks. In this case the side coincides with the tangent common line and the local frame is defined with respect to this line. In a detection algorithm,

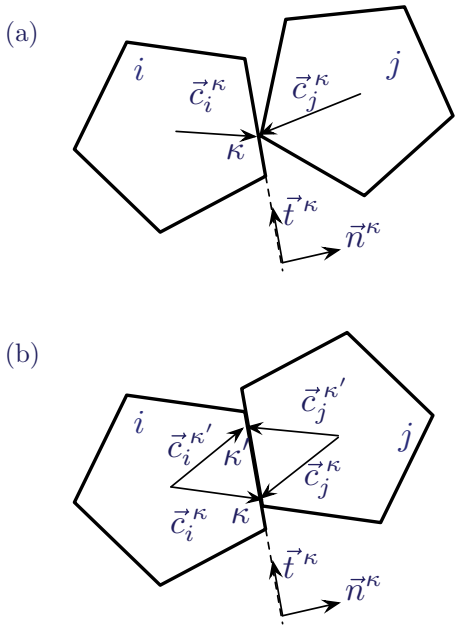

FIG. 1. (Color online) (a) Side-vertex contact and (b) side-side contact between two polygonal particles.

such as the *shadow overlap method* used in our simulations, a side-vertex contact corresponds to a single corner of a polygon crossing a side of a partner polygon [23,25,53]. Obviously, ideal contacts with no interpenetration of the particles ($\delta_n = 0$) would require infinite precision. In all numerical methods the detection of contact between two bodies consists actually in observing an overlap of the portions of space they occupy, so $\delta_n \leqslant 0$. These overlaps are a simple matter of geometrical precision in the framework of the CD method rather than a strain variable as in MD. The evolution of a granular system by a CD process is as much sensitive to such imperfections as that of a real system to the surface irregularities of real particles.

A side-side contact between two rigid polygons is equivalent to two geometrical constraxints and can thus be represented by two distinct point contacts located on the common side, which defines the common tangent line between the two polygons. For this reason we refer to side-side contacts as *double contacts*, in contrast to side-vertex contacts to which we refer as *simple contacts*. In practice, a double contact is detected when a double intrusion occurs between two polygons (two vertices of a polygon crossing the same side of another polygon or at least one vertex of each of the two polygons crossing a side of the other polygon). The common tangent line is defined as an intermediate line crossing the overlap zone between the two sides involved in the double contact and the projections of the intruding vertices onto this line are used to define two points representing the double contact. The algorithm is insensitive to the technical details of this choice as long as the intrusions are small compared to particle sizes, i.e., if the neighbor list is frequently updated and the time step is sufficiently small. For example, in our simulations the intrusion never exceeds 1% of particle diameter.

The two points of a double contact determined by the detection procedure obey Signorini's conditions and Coulomb's friction law (see the Appendix). However, the forces and displacements at the two points are coupled as a result of the rigidity of the particles, which imposes the equality of the sliding velocities. Let κ and κ' be two points belonging to a double contact between two polygons, as shown in Fig. 1. The contact frame $(\vec{n},\vec{t})$ is common to the two point contacts, but the contact vectors $\vec{c}_i^{\,\kappa}$ and $\vec{c}_j^{\,\kappa'}$ are different. If both contact points are persistent and nonsliding, the contact normal forces f_n^{κ} and $f_n^{\kappa'}$ and tangential forces f_t^{κ} and $f_t^{\kappa'}$ may take independent values compatible with Signorini's conditions ($f_n^{\kappa} \geqslant 0$, $f_n^{\kappa'} \geqslant 0$) and Coulomb's law of friction ($|f_t^{\kappa}| \leqslant \mu f_n^{\kappa}$, $|f_t^{\kappa'}| \leqslant \mu f_n^{\kappa'}$). However, if one of the two contacts is sliding, then the other contact must be sliding too, with the equality of the sliding velocities $u_t^{\kappa} = u_t^{\kappa'}$. This condition implies that f_t^{κ} and $f_t^{\kappa'}$ are of the same sign so that the sliding status is verified not only at each of the two contact points ($f_t^{\kappa} = \pm\mu f_n^{\kappa}$ and $f_t^{\kappa'} = \pm\mu f_n^{\kappa'}$) but also for the double contact, i.e., $f_t^{\kappa} + f_t^{\kappa'} = \pm\mu(f_n^{\kappa'} + f_n^{\kappa'})$.

Since the equations of dynamics are based on the rigid-body degrees of freedom, the equality of sliding velocities at the two points representing a double contact is in principle correctly calculated if the two points are handled as independent contacts in the iteration process. However, the number of iterations for convergence declines if the equality of the sliding velocities is enforced directly in the iteration process. To do so, Coulomb's friction law for a double contact is implemented

as follows:

$$
\begin{aligned}
u_t^\kappa > 0 &\Rightarrow \begin{cases} f_t^\kappa = -\mu f_n^\kappa \\ f_t^{\kappa'} = -\mu f_n^{\kappa'}, \quad u_t^{\kappa'} > 0; \end{cases} \\
u_t^\kappa = 0 \quad \text{or} \quad u_t^{\kappa'} = 0 &\Rightarrow \begin{cases} -\mu f_n^\kappa \leqslant f_t^\kappa \leqslant \mu f_n^\kappa \\ -\mu f_n^{\kappa'} \leqslant f_t^{\kappa'} \leqslant \mu f_n^{\kappa'}; \end{cases} \qquad (1) \\
u_t^\kappa < 0 &\Rightarrow \begin{cases} f_t^\kappa = \mu f_n^\kappa \\ f_t^{\kappa'} = \mu f_n^{\kappa'}, \quad u_t^{\kappa'} < 0. \end{cases}
\end{aligned}
$$

In practice, the inequalities (1) are implemented in the correction step when solving the local Signorini-Coulomb problem for a double contact between two particles (see the Appendix).

The two points attributed to a double contact and the calculated forces are only intermediate objects. The only physically meaningful forces acting at a double contact are the resultant forces $f_n = f_n^\kappa + f_n^{\kappa'}$ and $f_t = f_t^\kappa + f_t^{\kappa'}$. It is easily shown that $f_n \geqslant 0$ and $|f_t| \leqslant \mu f_n$ if the two contact points obey Signorini's conditions and Coulomb's friction law. Since only the force resultants and relative displacements are material at a double contact, the choice of the two representative points of a double contact is a matter of technical convenience with no real impact on the result.

Ideally, vertex-vertex contacts should never occur, but due to finite precision we do observe ambiguous situations that may be considered as vertex-vertex contacts, as shown in Fig. 2, and that require special treatment. The difficulty lies in the choice of a common tangent line and two representative points such that the subsequent particle motions under the effect of contact laws at those points do not lead to further mutual intrusion of the particles. The intrusion may increase due to both normal and tangential relative displacements with respect to the four sides involved in the vertex-vertex contact. This means that a vertex-vertex contact may be resolved either into two side-vertex contacts or into two side-side contacts and treated as described previously. An example is shown in Fig. 2, where two side-vertex contacts are defined to represent the intersecting vertices (exaggerated on the figure). This is a simple and robust method, although alternative methods for the choice of the common line and local frame may be proposed.

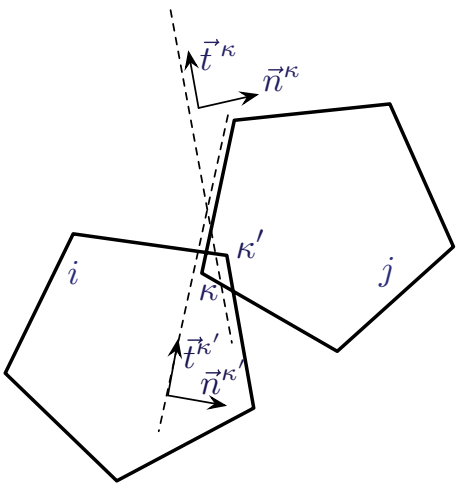

FIG. 2. Vertex-vertex intersection (exaggerated) resolved into two side-vertex contacts.

B. Description of the packings and the simple shear test

We prepared 13 different packings, each comprising 10 000 regular polygons with the same number of sides $n_s \in [3,4,\ldots,10,11,17,30,40,60]$. Additionally, we build one more packing composed of the same number of disks. The angularity $\alpha = 2\pi/n_s$ varies from 0 for disks to $2\pi/3$ for triangles. In order to avoid long-range ordering, we introduce size polydispersity by varying the circumradius of the polygons from $0.6\langle d\rangle$ to $2.4\langle d\rangle$, where $\langle d\rangle$ is the mean circumradius, with a uniform distribution by volume fractions.

The particles are initially placed in a semiperiodic box $100\langle d\rangle$ wide, using a geometrical procedure [54,55]. Then all packings are sheared by imposing a constant confining stress σ_{wall} and a constant horizontal velocity v_{wall} on the upper wall, as schematized in Fig. 3. To avoid strain localization at the boundaries and to guarantee that the shear strain is uniformly distributed in the bulk, the particles in contact with the walls are glued to them and the gravity is set to zero. The friction coefficient μ_s between particles is set to 0.4.

Since we are interested in the quasistatic (rate-independent) behavior, the particle inertia should be negligible compared to the confining pressure. From the shear rate $\dot{\gamma} = v_{\text{wall}}/y_{\text{wall}}$ and σ_{wall} an inertia parameter I is defined by Ref. [56]

$$
I = \dot{\gamma}\langle d\rangle\sqrt{\frac{\rho}{\sigma_{\text{wall}}}}, \qquad (2)
$$

where ρ is the mass density. Experiments and simulations show that this condition is fulfilled when $I < 10^{-3}$. In all our tests we have $\dot{\gamma} = 10^{-6}/\Delta t$ and $\sigma_{\text{wall}} = 10^{-4}\rho(\langle d\rangle\Delta t)^2$. Hence $I \sim 10^{-4}$, which means that our sheared samples can reasonably be considered to be in a quasistatic state.

The samples are sheared up to a large cumulative shear strain $\gamma = x_{\text{wall}}/y_{\text{wall}} = 4$, where x_{wall} is the horizontal displacement of the upper wall and y_{wall} is its vertical position. Figure 4 shows the stress ratio $\tau_{\text{wall}}/\sigma_{\text{wall}}$ and the normalized volume of the packing $V/\langle d\rangle^2$, as functions of the shear strain γ, for four different values of α, where τ_{wall} is the tangential

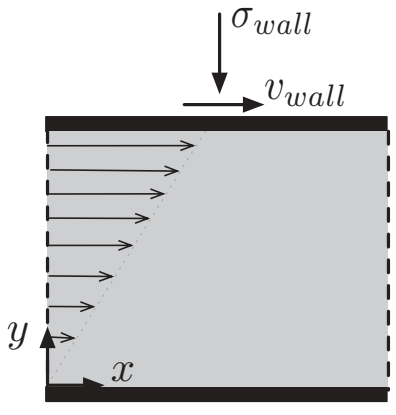

FIG. 3. Schematic representation of the simulated shear test; the dashed lines represent periodic boundaries. Here v_{wall} is the horizontal velocity of the wall and σ_{wall} is the confining pressure. The arrows inside the box represent the velocity field.

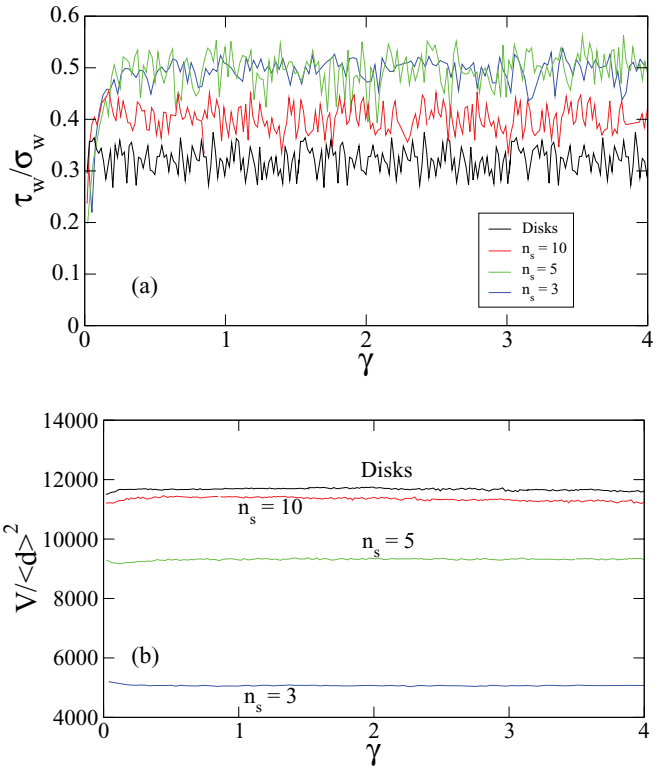

FIG. 4. (Color online) (a) Stress ratio $\tau_{\text{wall}}/\sigma_{\text{wall}}$ and (b) normalized volume of the packing $V/\langle d\rangle^2$ as functions of the shear strain γ for four different values of α.

stress at the moving wall. We see that the packings are in the steady state up to small fluctuations around a mean both for $\tau_{\text{wall}}/\sigma_{\text{wall}}$ and $V/\langle d\rangle^2$. In the following sections all average quantities represent the last 50% of cumulative shear strain so that they truly characterize the behavior of the system in the steady state [57]. Video samples of the simulations analyzed in this paper can be found in Ref. [58].

III. SHEAR STRENGTH AND PACKING FRACTION

The shear strength of a granular material is characterized by the coefficient of internal friction μ^*, which requires the stress tensor $\boldsymbol{\sigma}$ at any stage of deformation calculated from the simulation data, giving access to the contact network and forces. We start with the internal moment tensor $\boldsymbol{M}^p$ of each particle p, defined by

$$M_{ij}^p = \sum_{c\in p} f_i^c r_j^c, \tag{3}$$

where f_i^c is the i component of the force exerted on particle p at contact c, r_j^c is the j component of the position vector of the same contact, and the summation runs over all contacts c of particle p. The average stress tensor $\boldsymbol{\sigma}$ in a volume V of the granular assembly is defined by Ref. [59]

$$\boldsymbol{\sigma} = \frac{1}{V}\sum_{p\in V} \boldsymbol{M}^p = \frac{1}{V}\sum_{c\in V} f_i^c \ell_j^c, \tag{4}$$

where ℓ^c is the intercenter vector joining the centers of the two touching particles at the contact c. Note that the first summation runs over all particles whereas the second

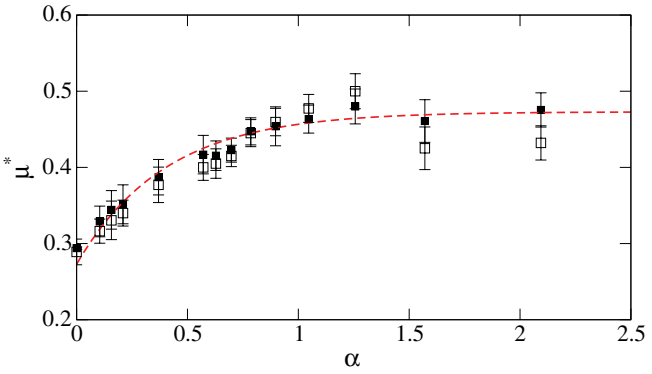

FIG. 5. (Color online) Coefficient of internal friction μ^* as a function of the angularity α evaluated directly from the numerical data (solid squares) and predicted by Eq. (8) (open squares). The error bars represent the standard deviation in the steady state.

summation involves all contacts in the volume V, with each contact appearing only once. The mean stress in two dimensions (2D) is given by $p = (\sigma_1 + \sigma_2)/2$ and the deviatoric stress is $q = (\sigma_1 - \sigma_2)/2$, where σ_1 and σ_2 are the principal stresses. The coefficient of internal friction in the steady state is defined by

$$\mu^* = \frac{q}{p}. \tag{5}$$

Figure 5 shows the evolution of μ^* as a function of the angularity α of the particles. The shear strength first increases with α from $\mu_0^* \simeq 0.29$ and then saturates for particles having 6 or fewer sides ($\alpha \geqslant 1.25$) for which $\mu_{\geqslant 1}^* \simeq 0.47$. The data are well fit to an exponential function:

$$\mu^* = \mu_0^* + (\mu_{\geqslant 1}^* - \mu_0^*)(1 - e^{-\alpha/\alpha_c}), \tag{6}$$

with $\alpha_c \simeq 0.6$. The fast increase of μ^* with α and its saturation is rather unexpected as it indicates that small deviations of the shape from the disk have a stronger effect on μ^* than the larger variations of angularity for a small number of sides. This point will be discussed in more detail when we analyze below the microstructure and force transmission.

Figure 6 shows the packing fraction ν^* as a function of α. We see that the packing fraction declines from $\nu_0^* \simeq 0.828$ (for the disk packing) and saturates to $\nu_{\geqslant 1}^* \simeq 0.798$. It is remarkable

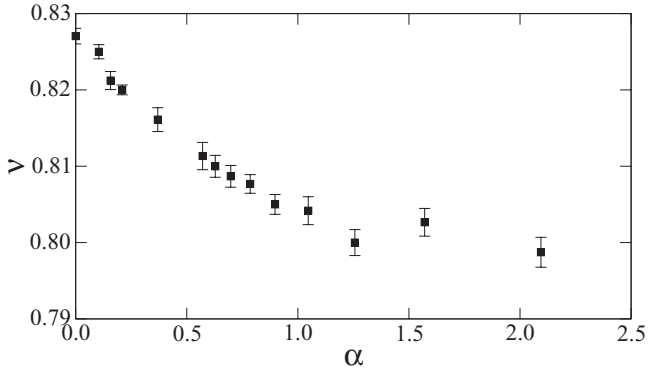

FIG. 6. Steady-state value of the packing fraction ν^* as a function of the angularity α. The error bars represent the standard deviation in the steady state.

that the packing fraction follows a trend opposite to that of the shear strength. These results represent a different example in which a decrease in packing fraction is accompanied by an increase in shear strength, as it was previously observed for packings of elongated and nonconvex particles [18,22]. In the following we analyze the microstructural properties of our packings of polygonal particles with the aim of identifying the origins of their shear strength.

IV. MICROMECHANICAL ANALYSIS

A. Connectivity

Figure 7 shows a snapshot of the contact network in the steady state for three samples of polygonal particles with $n_s = 10$, 5, and 3, as well as for the disk packing. We see that the contact network topology varies strongly with angularity. For example, the floating particles are organized in groups in the disk packings, whereas they are mostly isolated in the case of triangular particles. In contrast, the contact network becomes more connected as the angularity increases. At lowest order, the connectivity of the particles is characterized by the proportion κ of nonfloating particles and the coordination number z (average number of force-bearing contacts per particle). Figure 8 shows κ and z as functions of α. We see that κ and z decline (from 0.85 to 0.68 and from 3.25 to 3.15, respectively) as α increases, in accordance with the decrease of packing fraction shown in Fig. 6. However, the trend is reversed beyond $\alpha \simeq 1$ for both z and κ. In particular, we observe that z increases up to 3.5, which is higher than that in the disk packing. This increase suggests that the sharp corners of very angular particles allow for deep contacts between neighbors that are unreachable for less angular particles. These results show that for large angularities, the packings are looser but better connected.

The connectivity of the particles may be characterized in more detail by specifying the proportion P_c of particles having exactly c contacts. Note that only the force-bearing contacts are concerned. We have $P_0 = P_1 = 0$. Figure 9 shows P_c for $c = 2, \ldots, 8$ as a function of α in the steady state. For all values of α, with the exception of triangles and squares (i.e., for $\alpha = 2\pi/3$ and $\pi/2$ in the figure), P_3 prevails and it remains nearly constant below $\alpha \simeq 1.25$. Beyond $\alpha = 1.25$, it declines rapidly, contrary to all proportions P_c, which increase with α. We also observe that P_4 decreases slightly with α for $\alpha < 1.25$, whereas in the same range P_2 increases almost in the same proportion. Hence, as the angularity becomes higher, increasing numbers of particles are equilibrated by two opposite forces mostly acting at the side-side contacts. Finally, it is interesting to note that the proportions P_c of particles with more than four contacts remain nearly constant below $\alpha = 1.25$, but increase only slightly in number for squares and triangles. In this way, even a slight increase in angularity (with a disk as the reference shape) has a strong effect on the connectivity and mechanical behavior, as we already remarked with respect to the evolution of μ^* and ν^* in Figs. 5 and 6.

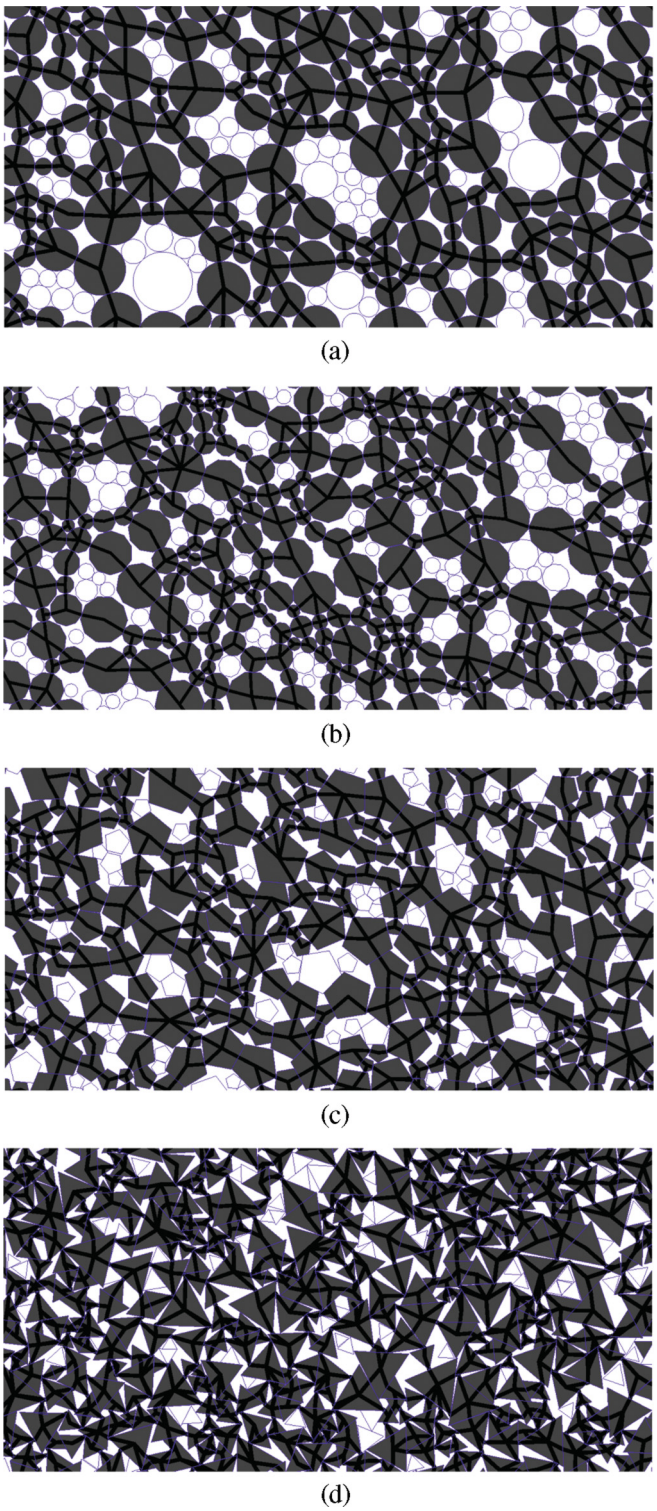

FIG. 7. (Color online) Snapshots of the contact network for three samples of polygonal particles with (b) $n_s = 10$, (c) $n_s = 5$, and (d) $n_s = 3$ and (a) for the disk packing. The floating particles (i.e., particles with one or no contact) are drawn in light gray and the contacts are represented by line segments joining the centers of mass of the particles with the contact points.

B. Anisotropy of the contact and force networks

The shear strength of granular materials is generally attributed to the buildup of an anisotropic structure induced by shearing. This anisotropy is basically related to the distribution of contact normals $\boldsymbol{n}$. Therefore, we may obtain a full description of the state of anisotropy by a partition of various

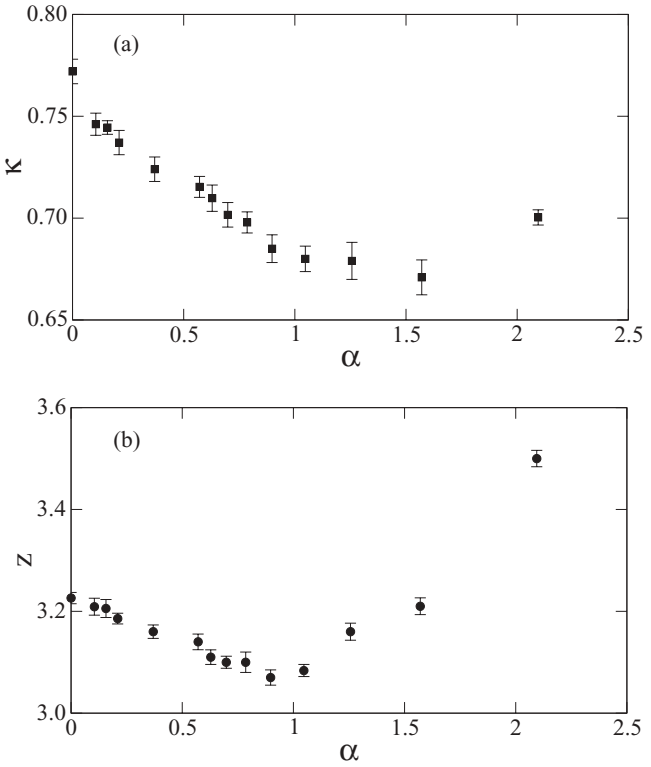

FIG. 8. (a) Proportion κ of nonfloating particles as a function of the angularity α. (b) Coordination number z as a function of the angularity α. The error bars represent the standard deviation in the steady state.

mechanical quantities according to the directions of contact normals. This amounts to replacing the space direction used in continuum mechanics for the representation of the stress and strain fields by the contact orientation.

The most basic descriptor of anisotropy is the probability distribution $P(\boldsymbol{n})$ of the contact normals, which is generically nonuniform. In two dimensions, the unit vector $\boldsymbol{n}$ is described by a single angle θ and the probability density $P(\theta)$ of contact orientations θ provides the required statistical information about the contact network. A local frame $(\boldsymbol{n},\boldsymbol{t})$ can be attached to each contact, where $\boldsymbol{t}$ is an orthonormal unit vector (see

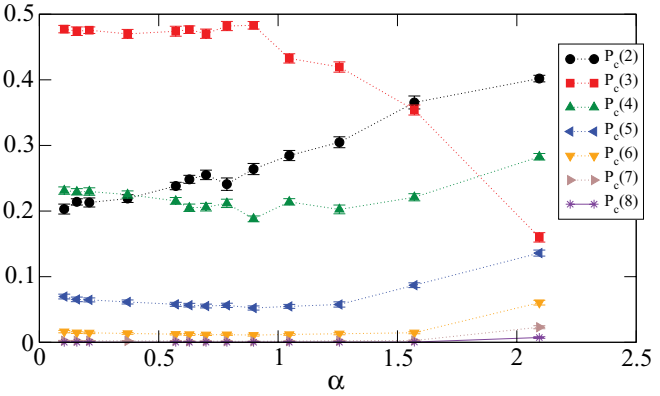

FIG. 9. (Color online) Connectivity of particles defined as the proportion $P_c(c)$ of particles with exactly c contacts as a function of α in the steady state.

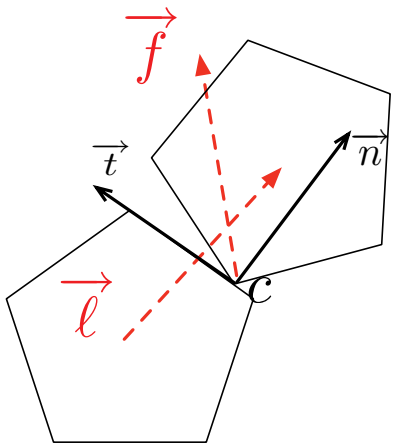

FIG. 10. (Color online) Local contact frame.

Fig. 10). The local geometry associated with the two contact neighbors is characterized by the branch vector $\boldsymbol{\ell}$ joining the particle centers. It can be projected in the local contact frame: $\boldsymbol{\ell} = \ell_n \boldsymbol{n} + \ell_t \boldsymbol{t}$. Note that, in contrast to circular particles, for which $\ell_t = 0$, in a packing of polygonal particles this component is nonzero. In the same way, the contact force $\boldsymbol{f}$ can be expressed in terms of its normal and tangential components: $\boldsymbol{f} = f_n \boldsymbol{n} + f_t \boldsymbol{t}$.

Along with $P(\theta)$, the anisotropy of the packing can be further characterized by the angular averages of the components of the branch vectors and contact forces as a function of the orientation θ: $\langle \ell_n \rangle(\theta)$, $\langle \ell_t \rangle(\theta)$, $\langle f_n \rangle(\theta)$, and $\langle f_t \rangle(\theta)$. These functions describe the general state of anisotropy and both experiments and simulations show that in a sheared granular material, they tend to take a simple unimodal shape, which can be well approximated by the lowest-order Fourier expansion [3,10,18,20,22,60–69]:

$$\begin{aligned} P(\theta) &= \frac{1}{2\pi}\{1 + a_c \cos 2(\theta - \theta_c)\}, \\ \langle \ell_n \rangle(\theta) &= \langle \ell_n \rangle\{1 + a_{ln} \cos 2(\theta - \theta_{ln})\}, \\ \langle \ell_t \rangle(\theta) &= \langle \ell_n \rangle a_{lt} \sin 2(\theta - \theta_{lt}), \\ \langle f_n \rangle(\theta) &= \langle f_n \rangle\{1 + a_{fn} \cos 2(\theta - \theta_{fn})\}, \\ \langle f_t \rangle(\theta) &= \langle f_n \rangle a_{ft} \sin 2(\theta - \theta_{ft}), \end{aligned} \tag{7}$$

where a_c is the contact orientation anisotropy, a_{ln} is the normal branch anisotropy, a_{lt} is the tangential branch anisotropy, a_{fn} is the normal force anisotropy, and a_{ft} is the tangential force anisotropy. The angles θ_c, θ_{ln}, θ_{lt}, θ_{fn}, and θ_{ft} are the corresponding privileged directions. These directions can all be different, but they coincide with the principal stress direction θ_σ in a sheared granular material, as illustrated in Fig. 11.

The anisotropies a_c, a_{ln}, a_{lt}, a_{fn}, and a_{ft} are interesting not only as descriptors of the granular microstructure and force transmission but more fundamentally because they add together to build the shear strength of the material. Indeed, from the expression (4) of the stress tensor, the following relationship can be easily established between the anisotropy

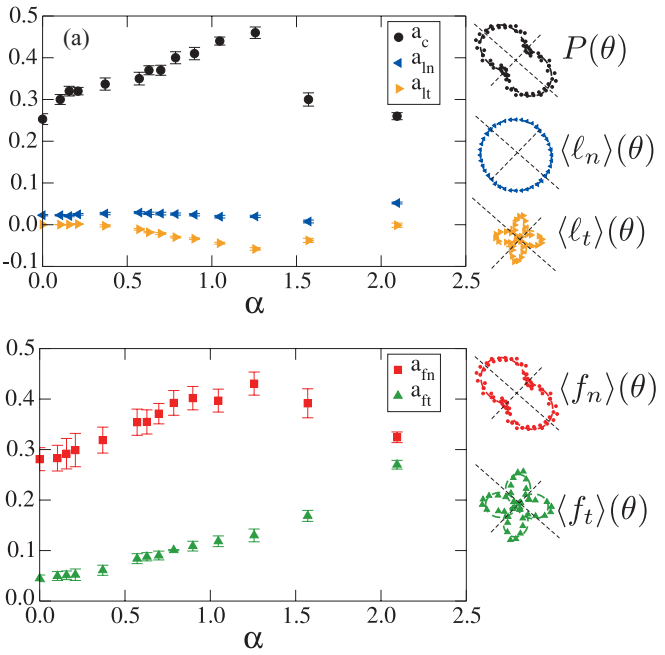

FIG. 11. (Color online) Evolution of the anisotropy parameters (a) a_c, a_{ln}, and a_{lt} and (b) a_{fn} and a_{ft} as functions of the particle shape angularity α. Error bars represent the standard deviation in the steady state. The polar diagrams of the corresponding angular distributions are shown for $\alpha \simeq 1$ (i.e., $n_s = 6$) together with their Fourier expansion [i.e., Eq. (7)].

parameters and the stress ratio q/p [3,18]:

$$\frac{q}{p} \simeq \frac{1}{2}(a_c + a_{ln} + a_{lt} + a_{fn} + a_{ft}), \tag{8}$$

where the cross products between the anisotropy parameters have been neglected. The stress ratio q/p given by this expression from the anisotropy parameters measured from the numerical data is shown in Fig. 5 as a function of α together with those given by direct measurement. We see that Eq. (8) provides a nice approximation of the shear strength for all values of α.[1]

The evolution of the five anisotropies with α is shown in Fig. 11. The normal and tangential branch anisotropies a_{ln} and a_{lt} are negligible in comparison to the other anisotropy parameters. This is due to the absence of shape eccentricity of the particles [18,70] and to the low span in the particle size distribution [67]. The other anisotropies a_c, a_{fn}, and a_{ft} grow as α increases from zero (for the disk packing) up to $\alpha \simeq 1.25$ (for the hexagon packing). This increase of all anisotropies underlies the observed increase in the internal angle of friction in this range. In contrast, the increase of the anisotropies reflects the increasing number of side-side contacts, which capture the strong force chains and form columnlike structures, which can be stable without sidewise support (see below).

For polygons with fewer than six sides ($\alpha \geqslant 1.25$), a rapid decrease of a_c and a_{fn} occurs, whereas a_{ft} grows at the same time. As observed in Fig. 11, this increase of a_{ft} is large enough to additively compensate for [see Eq. (8)] the decrease of a_c and a_{fn}, so that the shear strength remains nearly constant in this range of α, as observed in Fig. 5.

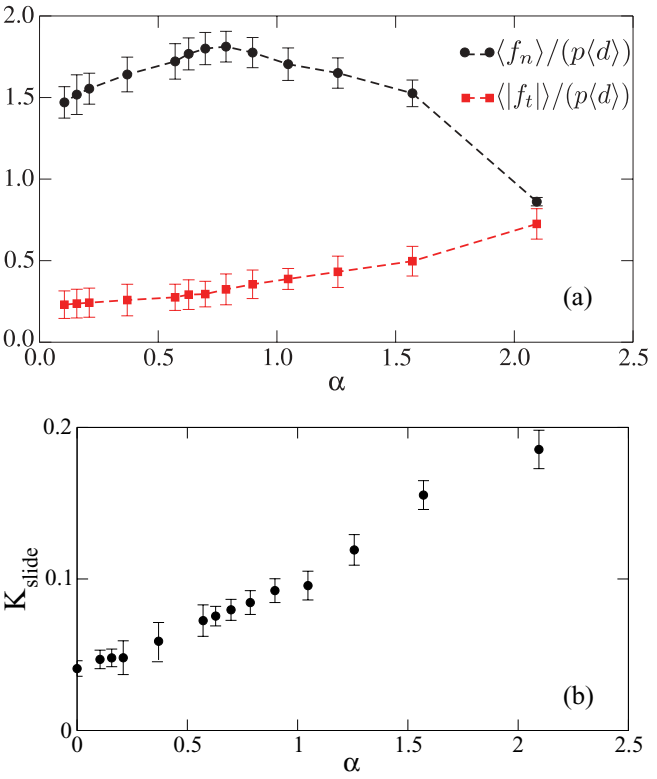

FIG. 12. (Color online) (a) Mean normal force $\langle f_n \rangle$ and mean tangential force $\langle |f_t| \rangle$ normalized by $p\langle d \rangle$ as functions of the angularity α. (b) Proportion k_{slide} of sliding contacts as a function of α. The error bars represent the standard deviation in the steady state.

The decrease of a_c for $\alpha \geqslant 1.25$ is related to the increase of the coordination number z as shown in Fig. 8(b). Indeed, higher values of z imply higher dispersion of contact orientations. In contrast, the increase of a_{ft} may be attributed to the fact that the rotational mobility of the particles is strongly reduced as a result of enhanced angular exclusions due to shape angularity so that the particles tend to slide rather than rolling with a strong increase of friction mobilization [68]. At the same time, a_{fn} declines naturally as the friction forces take part more actively in force transmission. This is indeed what we observe in Fig. 12, which shows the mean normal force $\langle f_n \rangle$ and mean tangential force $\langle |f_t| \rangle$, as well as the proportion k_{slide} of sliding contacts (i.e., contacts in which $|f_t| = \mu |f_n|$), as functions of α. Both $\langle f_n \rangle$ and $\langle |f_t| \rangle$ initially increase with α, but $\langle f_n \rangle$ declines beyond $\alpha \gtrsim 1$ whereas $\langle |f_t| \rangle$ keeps increasing. The proportion of sliding contacts rises as the particles become increasingly angular and takes values as high as 0.2, i.e., nearly 4 times above those measured in the packing composed of disks ($\alpha = 0$).

C. Role of side-vertex and side-side contacts

As mentioned in the preceding section, the distinctive features of a material composed of polygonal particles are explained by the possibility of forming side-side contacts. It is

[1] A similar relation can be obtained in 3D using spherical harmonics [10,70].

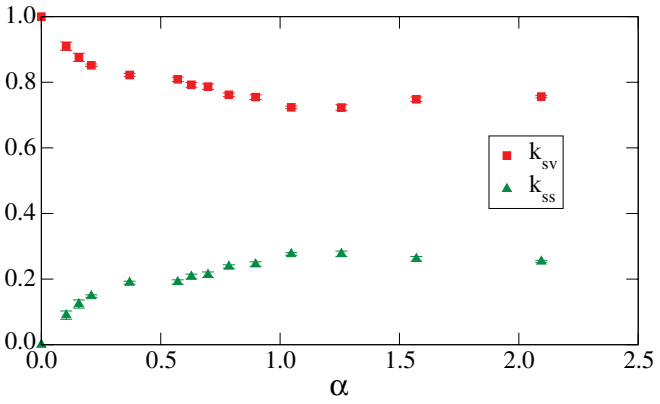

FIG. 13. (Color online) Proportions of side-side (ss) and side-vertex (sv) contacts as functions of the angularity α. The error bars represent the standard deviation in the steady state.

thus interesting to investigate the relative roles of the two types of contacts, i.e., side-vertex (sv) and side-side (ss) contacts, with respect to the shear strength and anisotropy. Figure 13 shows the proportions k_{sv} and k_{ss} of sv and ss contacts, respectively, as a function of α. Irrespective of angularity, the sv contacts prevail in the contact network. However, k_{sv} decreases from 1 for the disks ($\alpha = 0$) down to $\simeq 0.75$ for $\alpha \gtrsim 1.25$ and remains practically constant for more angular particles.

Figure 14 shows a snapshot of the normal force network disk packing as well as three snapshots of the packings with $n_s = 10$, 5, and 3. The force lines connect particle centers to the contacts and their thickness is proportional to the normal force. For $n_s = 10$ and 5, the ss contacts appear often in distinctive force chains. However, for $n_s = 3$ (triangles), despite approximately the same proportion k_{ss}, the ss contact forces are much more diffuse and intricately mixed with sv contacts. This visual impression is consistent with the decrease of a_n observed in Fig. 11.

The stress tensor can be partitioned as a sum of two tensors representing the respective contributions of sv and ss contacts by considering the expression (4) of the stress tensor and restricting the summation to each contact type:

$$\boldsymbol{\sigma} = \boldsymbol{\sigma}_{sv} + \boldsymbol{\sigma}_{ss}, \tag{9}$$

where

$$(\sigma_{sv})_{ij} = \frac{1}{V} \sum_{c \in \mathcal{A}(sv)} \ell_i f_j, \quad (\sigma_{ss})_{ij} = \frac{1}{V} \sum_{c \in \mathcal{A}(ss)} \ell_i f_j, \tag{10}$$

with $\mathcal{A}(sv)$ and $\mathcal{A}(ss)$ the sets of sv and ss contacts, respectively. Figure 15 displays the evolution of q/p, q_{sv}/p, and q_{ss}/p as a function of α. It is seen that q_{sv}/p is nearly constant and $\simeq 0.24$, except for the packing of triangular particles in which $q_{sv}/p \simeq 0.35$. In contrast, q_{ss}/p first increases with α from 0 to $\simeq 0.3$ for pentagons and then declines to 0.2 for squares and 0.1 for triangles. This shows that the variation of the shear strength is mostly governed by the contribution of side-side contacts, even if their proportion is low. This profound effect of faceted grain shapes on stress transmission has been previously shown both experimentally and numerically [17–20].

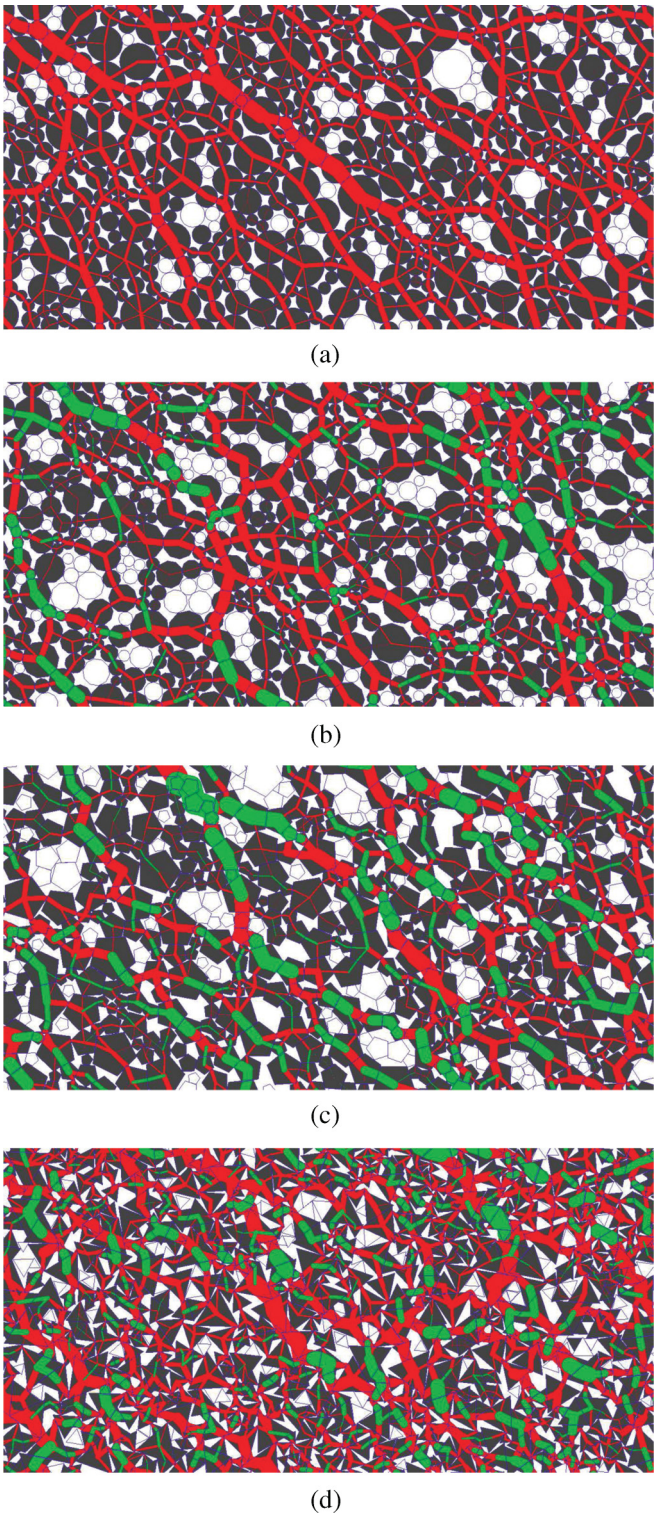

FIG. 14. (Color online) Snapshots of (a) the packing of disks and the packings of polygons with (b) $n_s = 10$, (c) $n_s = 5$, and (d) $n_s = 3$ in the steady state. The sv contacts are in red (dark gray) and ss contacts are in green (light gray). The line thickness is proportional to the normal force.

Along the same lines, we may also evaluate the partial contact and force anisotropies $a_{c\gamma}$, $a_{ln\gamma}$, $a_{lt\gamma}$, $a_{fn\gamma}$, and $a_{ft\gamma}$, where γ stands either for ss or for sv. Since the privileged

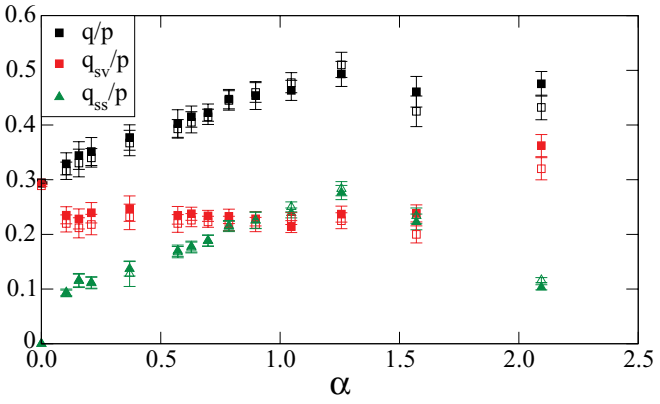

FIG. 15. (Color online) Total shear strength (q/p) and partial shear strengths for side-vertex (sv) and side-side (ss) contacts as functions of the angularity α, together with the values predicted by Eq. (8) (open symbols). The error bars represent the standard deviation in the steady state.

directions of the partial angular functions describing the γ contacts and forces are practically the same as the overall privileged direction for all contacts and forces, the total contact and force anisotropies are given by the sum of the corresponding partial anisotropies. The partial contact and forces anisotropies are shown in Figs. 16 and 17 as functions of α together with the total anisotropies. Note that Eq. (8) is also verified when restricted to γ contacts. We see that $a_{csv} \simeq a_{fnsv} \simeq 0.2$ and $a_{ftsv} \simeq 0.05$ for all α. In other words, the variation of the total anisotropy is mainly governed by that of the anisotropies developed by side-side contacts. The stress plateau discussed previously for the whole contact network for higher angularity is due to the falloff of a_{css} and a_{fnss} for squares and triangles compensated for by the increase of the partial tangential force anisotropy of side-side contacts a_{ftss}. This shows the crucial role of side-side contacts in stress transmission and mobilization of internal friction for most angular particles.

V. CONCLUSION

In this paper we investigated the effect of particle shape angularity on the quasistatic behavior of sheared granular

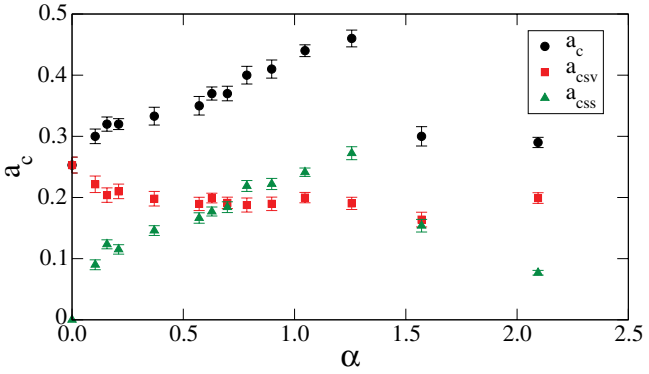

FIG. 16. (Color online) Partial contact orientation anisotropies a_{css} and a_{csv} of ss and sv contacts as functions of the angularity α. The error bars represent the standard deviation in the steady state.

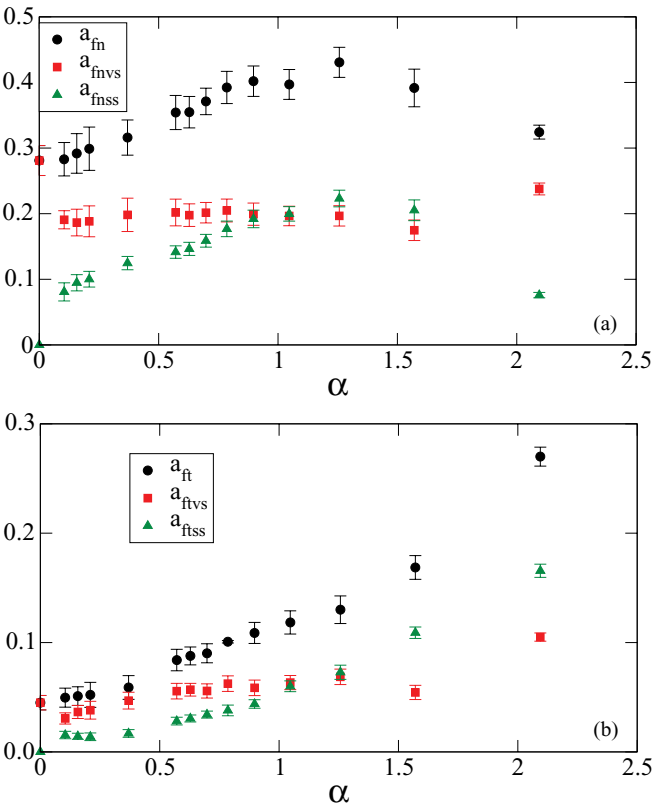

FIG. 17. (Color online) (a) Partial normal force anisotropies a_{fnss} and a_{fnsv} and (b) partial tangential force anisotropies a_{ftss} and a_{ftsv} of ss and sv contacts as functions of the angularity α. The error bars represent the standard deviation in the steady state.

materials by means of contact dynamics simulations. The particles are regular polygons characterized by their angularity. The macroscopic and microstructural properties of several packings of 10^4 particles in simple shear conditions were analyzed as a function of angularity in the steady state.

We expected the steady-state internal friction coefficient to decrease rapidly for decreasing angularity and tend to a nearly constant value close to that of a disk packing. Instead, our numerical simulations reveal a nearly constant value of the internal friction coefficient for most angular polygons (triangles, squares, and pentagons) and a rapid decrease as angularity is reduced. Similar behavior was also observed for the packing fraction and several descriptors of the microstructure such as the coordination number and anisotropy parameters. This counterintuitive observation shows that a slight increase in angularity (with a disk as the reference shape) has a strong influence on the mechanical behavior. In this respect, the effect of a low angularity seems to be as strong as that of surface roughness and friction coefficient between particles.

For polygons with the highest angularity, i.e., for polygons of 3–5 sides, a different mechanism is observed. In particular, the coordination number declines as angularity increases, except for highly angular particles, for which it rises. In the latter case, the contact orientation anisotropy and normal force anisotropy decline as angularity increases, whereas the tangential force anisotropy increases. The compensation

between these effects leads to a nearly constant shear strength. The friction mobilization appears as a key parameter for the shear strength of angular particles. It grows smoothly with angularity and, mainly at side-side contacts, it is responsible for the increasing shear strength of the material.

In this work the friction coefficient between particles was kept at a constant value for all angularities. It would be highly instructive to assess the proper role of friction by varying this parameter systematically for each angularity. A similar investigation can also be performed with irregular polygons in 2D and polyhedra in 3D, making it possible to explore the implications of these results in the context of practical applications

ACKNOWLEDGMENTS

We thank in particular Alfredo Taboada for fruitful discussions and Frédéric Dubois for assistance with the LMGC90 platform used for the simulations. We acknowledge financial support from the Ecos-Nord program (Grant No. C12PU01).

APPENDIX: CONTACT DYNAMICS METHOD

In this Appendix we briefly describe the CD method in 2D by adapting a detailed description given in Ref. [71]. The implementation of the CD method with polygonal particles is described in Sec. II.

1. Contact laws

Let us consider two particles i and j with a contact at a point κ within a granular material. We assume that a unique common line (plane in 3D) tangent to the two particles at κ can be geometrically defined so that the contact can be endowed with a local reference frame defined by a unit vector $\vec{n}$ normal to the common line and a unit vector $\vec{t}$ along the tangent line with an appropriate choice of the orientations of the axes.

Geometrically, a contact potentially exists if the gap δ_n between two particles is so small that within a small time interval δt (time step in numerical simulations) a collision may occur between the two particles. If the contact is effective, i.e., for $\delta_n = 0$, a repulsive (positive) normal force f_n may appear at κ with a value depending on the particle velocities and contact forces acting on the two partners by their neighboring particles (see Fig. 18). However, if δ_n is positive (a gap), the potential contact is not effective and f_n at the potential contact κ is identically zero. These disjunctive conditions can be described by the following inequalities:

$$\delta_n > 0 \Rightarrow f_n = 0, \quad \delta_n = 0 \Rightarrow f_n \geqslant 0. \tag{A1}$$

The important point about this relation between δ_n and f_n, called Signorini's conditions, is that it cannot be reduced to a (monovalued) function.

Signorini's conditions imply that the normal force vanishes when the contact is not effective. However, the normal force may vanish also at an effective contact. In particular, this is the case for $u_n = \dot{\delta}_n > 0$, i.e., for incipient contact opening. Otherwise, the effective contact is *persistent* and we have $u_n = \dot{\delta}_n = 0$. Hence Signorini's conditions can be split as follows:

$$\delta_n > 0 \Rightarrow f_n = 0, \quad \delta_n = 0 \wedge \begin{cases} u_n > 0 \Rightarrow f_n = 0 \\ u_n = 0 \Rightarrow f_n \geqslant 0. \end{cases} \tag{A2}$$

We see that for an effective contact, i.e., for $\delta_n = 0$, Signorini's conditions hold for the variables u_n and f_n.

Like Signorini's conditions, the Coulomb law of dry friction at an effective contact point can be expressed by a set of alternative inequalities for the friction force f_t and the sliding velocity u_t:

$$\begin{aligned} &u_t > 0 \Rightarrow f_t = -\mu f_n, \\ &u_t = 0 \Rightarrow -\mu f_n \leqslant f_t \leqslant \mu f_n, \\ &u_t < 0 \Rightarrow f_t = \mu f_n, \end{aligned} \tag{A3}$$

where μ is the coefficient of friction and it is assumed that the unit tangent vector $\boldsymbol{t}$ points in the direction of the sliding velocity so that $\vec{u}_t \cdot \vec{t} = u_t$. Like Signorini's conditions, this is a degenerate law that cannot be reduced to a (monovalued) function between u_t and f_t.

Signorini's conditions [Eq. (A2)] and Coulomb's friction law [Eq. (A3)] are represented as two graphs in Fig. 19 for an effective contact between two particles. We refer to these graphs as contact laws in the sense that they characterize the relation between relative displacements and forces irrespective of the rheology (viscoelastic or plastic nature) of the particles. These contact laws should be contrasted with force laws (employed in MD simulations), which describe a functional dependence between deformations (attributed to the contact point) and forces that is extracted from the material behavior of the particles. The force laws often employed in MD may also be considered as a regularization of the contact laws, in which the vertical branch in Signorini's and Coulomb's graphs is replaced by a steep linear or nonlinear function.

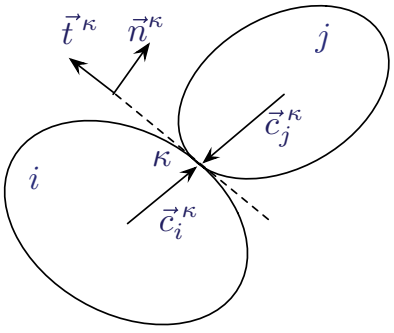

FIG. 18. (Color online) Geometry of a contact κ between two particles i and j with contact vectors $\vec{c}_i^{\kappa}$ and $\vec{c}_j^{\kappa}$ and contact frame $(\vec{n}^{\kappa},\vec{t}^{\kappa})$.

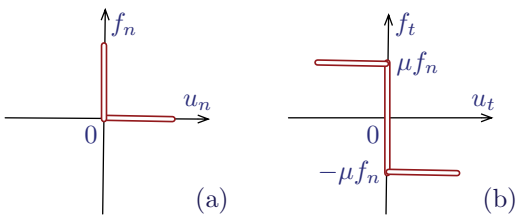

FIG. 19. (Color online) Graphs of (a) Signorini's conditions and (b) Coulomb's friction law.

2. Augmented contact laws

The use of contact laws in the CD method is consistent with the idea of a discrete model defined only at the scale of particle motions and involving no small subparticle length or force scales inherent to the force laws. However, such a coarse-grained model of particle motion implies nonsmooth dynamics, i.e., possible discontinuities in particle velocities and forces arising from collisions and variations of the contact status (effective or not, persistent or not, sliding or not). Such *events* occur frequently in granular flows and hence the approximation of the contact force f_n during δt is a *measure* problem in the mathematical sense [32,72]. A static or regular force f^s is the density of the measure $f^s\,dt$ with respect to time differential dt. In contrast, an impulse p generated by a collision has no density with respect to dt. In other words, the forces at the origin of the impulse are not resolved at the scale δt. In practice, however, we cannot differentiate these contributions in a coarse-grained dynamics and the two contributions should be summed up to a single measure and the contact force is defined as the average of this measure over δt.

In a similar vein, the left-limit velocities u_n^- and u_t^- at time t are not always related by a smooth variation (acceleration multiplied by the time step δt) with the right-limit velocities u_n^+ and u_t^+ at $t+\delta t$. Hence we assume that the contact laws [Eqs. (A2) and (A3)] are satisfied for a weighted mean of the relative left-limit and right-limit velocities:

$$u_n = \frac{u_n^+ + e_n\,u_n^-}{1+e_n}, \tag{A4}$$

$$u_t = \frac{u_t^+ + e_t\,u_t^-}{1+e_t}. \tag{A5}$$

The physical meaning of the coefficients e_n and e_t is best illustrated by considering a binary collision between two particles. A binary collision corresponds to an effective contact occurring in the interval $[t,t+\delta t]$ and a persistent contact in the sense of the mean velocity u_n. In other words, we have $u_n = 0$ and thus $-u_n^+/u_n^- = e_n$. Hence e_n can be identified with the normal restitution coefficient. In the same way, for $u_t = 0$, corresponding to a nonsliding condition (adherence of the two particles during their contact) implies $-u_t^+/u_t^- = e_t$, which is the tangential restitution coefficient. We see that when Signorini's and Coulomb's graphs are used with the mean velocities given by Eqs. (A4) and (A5), a contact is persistent in terms of u_n^+ (i.e., $u_n^+ = 0$) only if $e_n = 0$.

When a collision is not binary, the generated impulses propagate through the contact network so that a contact may experience several successive impulses during δt. Such events can be resolved for a sufficiently small time increment δt or they may be tracked according to an event-driven scheme. The event-tracking strategy is, however, numerically inefficient, of limited applicability, and in contradiction with the scope of the CD method based on coarse-grained dynamics. The use of mean velocities [Eqs. (A4) and (A5)] with the contact laws should thus be considered as a generalization of restitution coefficients to multiple collisions and contact networks for which the right-limit velocities u_n^+ and u_t^+ are not simply given by the left-limit velocities multiplied by the coefficients of restitution as in binary collisions but by combining the contact laws with the equations of dynamics.

3. Nonsmooth motion

The rigid-body motion of the particles is governed by Newton's equations under the action of imposed external bulk or boundary forces $\vec{F}_{\rm ext}$ and the contact reaction forces $\vec{f}^{\kappa}$ exerted by neighboring particles at the contact points κ. An absolute reference frame with unit vectors $(\hat{x},\,\hat{y})$ is assumed and we set $\hat{z} = \hat{x}\times\hat{y}$. Each particle is characterized by its mass m, moment of inertia I, mass center coordinates $\vec{r}$, mass center velocity $\vec{U}$, angular coordinates θ, and angular velocity $\omega\hat{z}$. For a smooth motion (twice differentiable), the equations of motion of a particle are

$$m\dot{\vec{U}} = \vec{F} + \vec{F}_{\rm ext}, \quad I\dot{\omega} = \mathcal{M} + \mathcal{M}_{\rm ext}, \tag{A6}$$

where $\vec{F} = \sum_\kappa \vec{f}^{\kappa}$ and $\mathcal{M} = \hat{z}\cdot\sum_\kappa \vec{c}^{\kappa}\times\vec{f}^{\kappa}$, with $\vec{c}^{\kappa}$ the *contact vector* joining the center of mass to the contact κ and $\mathcal{M}_{\rm ext}$ representing the moment of external forces.

For a nonsmooth motion with time resolution δt involving impulses and velocity discontinuities, an integrated form of the equations of dynamics should be used. Hence the equations of dynamics should be written as an equality of measures

$$m\,d\vec{U} = d\vec{F}' + \vec{F}_{\rm ext}dt, \quad I\,d\omega = d\mathcal{M}' + \mathcal{M}_{\rm ext}dt, \tag{A7}$$

where $d\vec{F}' = \sum_\kappa d\vec{f}'^{\kappa}$ and $d\mathcal{M}' = \hat{z}\cdot\sum_\kappa \vec{c}^{\kappa}\times d\vec{f}'^{\kappa}$. These measure differential equations can be integrated over δt with the definitions of $\vec{F}$ and $\mathcal{M}$ as approximations of the integral of $d\vec{F}'$ and $d\mathcal{M}'$. With these definitions, the integration of Eq. (A7) over δt yields

$$\begin{aligned} m(\vec{U}^+ - \vec{U}^-) &= \delta t\,\vec{F} + \delta t\,\vec{F}_{\rm ext},\\ I(\omega^+ - \omega^-) &= \delta t\,\mathcal{M} + \delta t\,\mathcal{M}_{\rm ext}, \end{aligned} \tag{A8}$$

where $(\vec{U}^-,\omega^-)$ and $(\vec{U}^+,\omega^+)$ are the left-limit and right-limit velocities of the particle, respectively.

The equations of dynamics can be written in a compact form for a set of N_p particles by using matrix representation. The particles are labeled with integers $i\in[1,N_p]$. The forces and force moments $F_x^i, F_y^i, \mathcal{M}^i$ acting on the particles i are arranged in a single high-dimensional column vector represented by a boldface letter $\boldsymbol{F}$ belonging to $\mathbb{R}^{3N_p}$. In the same way, the external bulk forces $F_{{\rm ext},x}, F_{{\rm ext},y}, \mathcal{M}_{\rm ext}$ applied on the particles and the particle velocity components U_x^i, U_y^i, ω^i are represented by column vectors $\boldsymbol{F}_{\rm ext}$ and $\boldsymbol{U}$, respectively. The particle masses and moments of inertia define a diagonal $3N_p\times 3N_p$ matrix denoted by $\boldsymbol{M}$. With these notations, the equations of dynamics (A8) are cast into a single matrix equation

$$\boldsymbol{M}(\boldsymbol{U}^+ - \boldsymbol{U}^-) = \delta t(\boldsymbol{F} + \boldsymbol{F}_{\rm ext}). \tag{A9}$$

4. Transfer equations

Since the contact laws are expressed in contact variables (u_n, u_t, f_n, and f_t), we need to express Eq. (A9) in the same variables. The contacts are labeled with integers $\kappa\in[1,N_c]$, where N_c is the total number of contacts. Like particle velocities, the contact velocities u_n^κ and u_t^κ can be collected in a column vector $\boldsymbol{u}\in\mathbb{R}^{2N_c}$. In the same way, the contact forces f_n^κ and f_t^κ are represented by a vector $\boldsymbol{f}\in\mathbb{R}^{2N_c}$. We

would like to transform the equations of dynamics from $\boldsymbol{F}$ and $\boldsymbol{U}$ to $\boldsymbol{f}$ and $\boldsymbol{u}$. The formal transformation of matrix equations [Eq. (A9)] is straightforward. Since the contact velocities $\boldsymbol{u}$ are linear in particle velocities $\boldsymbol{U}$, the transformation of the velocities is an affine application:

$$\boldsymbol{u} = \boldsymbol{G}\boldsymbol{U}, \tag{A10}$$

where $\boldsymbol{G}$ is a $2N_c \times 3N_p$ matrix containing basically information about the geometry of the contact network. A similar linear application relates $\boldsymbol{f}$ to $\boldsymbol{F}$:

$$\boldsymbol{F} = \boldsymbol{H}\boldsymbol{f}, \tag{A11}$$

where $\boldsymbol{H}$ is a $3N_p \times 2N_c$ matrix. We refer to $\boldsymbol{H}$ as *contact matrix*. It contains the same information as $\boldsymbol{G}$ in a dual or symmetric manner. It can easily be shown that $\boldsymbol{H} = \boldsymbol{G}^T$, where $\boldsymbol{G}^T$ is the transpose of $\boldsymbol{G}$. This property can be inferred from the equivalence between the power $\boldsymbol{F}\cdot\boldsymbol{U}$ developed by generalized forces $\boldsymbol{F}$ and the power $\boldsymbol{f}\cdot\boldsymbol{u}$ developed by the bond forces $\boldsymbol{f}$. In general, the matrix $\boldsymbol{H}$ is singular and by definition its null space has a dimension equal to at least $2N_c - 3N_p$.

The matrix $H^{i\kappa}$ can be decomposed into two matrices $H_n^{i\kappa}$ and $H_t^{i\kappa}$ such that

$$u_n^\kappa = \sum_i H_n^{T,\kappa i} U^i, \quad u_t^\kappa = \sum_i H_t^{T,\kappa i} U^i, \tag{A12}$$

and

$$F^i = \sum_\kappa \left(H_n^{i\kappa} f_n^\kappa + H_t^{i\kappa} f_t^\kappa \right). \tag{A13}$$

Using these relations, Eq. (A9) can be transformed into two equations for each contact κ:

$$\begin{aligned} &u_n^{\kappa+} - u_n^{\kappa-} \\ &\quad = \delta t \sum_{i,j} H_n^{T,\kappa i}\, M^{-1,ij} \left\{ \sum_\lambda \left(H_n^{j\lambda} f_n^\lambda + H_t^{j\lambda} f_t^\lambda \right) + F_{\text{ext}}^j \right\}, \\ &u_t^{\kappa+} - u_t^{\kappa-} \\ &\quad = \delta t \sum_{i,j} H_t^{T,\kappa i}\, M^{-1,ij} \left\{ \sum_\lambda \left(H_n^{j\lambda} f_n^\lambda + H_t^{j\lambda} f_t^\lambda \right) + F_{\text{ext}}^j \right\}. \end{aligned} \tag{A14}$$

We can now make linear relations between the contact variables from Eq. (A14) and definitions (A4) and(A5) appear explicitly. We set

$$\mathcal{W}_{k_1k_2}^{\kappa\lambda} = \sum_{i,j} H_{k_1}^{T,\kappa i} M^{-1,ij} H_{k_2}^{j\lambda}, \tag{A15}$$

where k_1 and k_2 stand for n or t. With this notation, Eqs. (A14) can be rewritten as follows:

$$\begin{aligned} &\frac{1+e_n}{\delta t}\left(u_n^\kappa - u_n^{\kappa-}\right) \\ &\quad = \mathcal{W}_{nn}^{\kappa\kappa} f_n^\kappa + \mathcal{W}_{nt}^{\kappa\kappa} f_t^\kappa + \sum_{\lambda(\neq\kappa)} \left\{ \mathcal{W}_{nn}^{\kappa\lambda} f_n^\lambda + \mathcal{W}_{nt}^{\kappa\lambda} f_t^\lambda \right\} \\ &\qquad + \sum_{i,j} H_n^{T,\kappa i} M^{-1,ij} F_{\text{ext}}^j, \end{aligned} \tag{A16}$$

$$\begin{aligned} &\frac{1+e_t}{\delta t}\left(u_t^\kappa - u_t^{\kappa-}\right) \\ &\quad = \mathcal{W}_{tn}^{\kappa\kappa} f_n^\kappa + \mathcal{W}_{tt}^{\kappa\kappa} f_t^\kappa + \sum_{\lambda(\neq\kappa)} \left\{ \mathcal{W}_{tn}^{\kappa\lambda} f_n^\lambda + \mathcal{W}_{nt}^{\kappa\lambda} f_t^\lambda \right\} \\ &\qquad + \sum_{i,j} H_t^{T,\kappa i} M^{-1,ij} F_{\text{ext}}^j. \end{aligned} \tag{A17}$$

The coefficients $\mathcal{W}_{k_1k_2}^{\kappa\kappa}$ for each contact κ can be calculated as functions of the contact network geometry and inertia parameters of the two partners 1_κ and 2_κ of the contact κ. Let $\vec{c}_i^{\,\kappa}$ be the contact vector joining the center of mass of particle i to the contact κ. The following expressions are easily established:

$$\begin{aligned} \mathcal{W}_{nn}^{\kappa\kappa} &= \frac{1}{m_{1_\kappa}} + \frac{1}{m_{2_\kappa}} + \frac{\left(c_{1t}^\kappa\right)^2}{I_{1_\kappa}} + \frac{\left(c_{2t}^\kappa\right)^2}{I_{2_\kappa}}, \\ \mathcal{W}_{tt}^{\kappa\kappa} &= \frac{1}{m_{1_\kappa}} + \frac{1}{m_{2_\kappa}} + \frac{\left(c_{1n}^\kappa\right)^2}{I_{1_\kappa}} + \frac{\left(c_{2n}^\kappa\right)^2}{I_{2_\kappa}}, \\ \mathcal{W}_{nt}^{\kappa\kappa} &= \mathcal{W}_{tn}^{\kappa\kappa} = \frac{c_{1n}^\kappa c_{1t}^\kappa}{I_{1_\kappa}} + \frac{c_{2n}^\kappa c_{2t}^\kappa}{I_{2_\kappa}}, \end{aligned} \tag{A18}$$

where $c_{in}^\kappa = \vec{c}_i^{\,\kappa}\cdot\vec{n}^\kappa$ and $c_{it}^\kappa = \vec{c}_i^{\,\kappa}\cdot\vec{t}^\kappa$ are the components of the contact vectors in the contact frame. The coefficients $\mathcal{W}_{k_1k_2}^{\kappa\kappa}$ are inverse reduced inertia.

An alternative representation of Eqs. (A16) and (A17) is the following:

$$\mathcal{W}_{nn}^{\kappa\kappa} f_n^\kappa + \mathcal{W}_{nt}^{\kappa\kappa} f_t^\kappa = (1+e_n)\frac{1}{\delta t} u_n^\kappa + a_n^\kappa, \tag{A19}$$

$$\mathcal{W}_{tt}^{\kappa\kappa} f_t^\kappa + \mathcal{W}_{tn}^{\kappa\kappa} f_n^\kappa = (1+e_t)\frac{1}{\delta t} u_t^\kappa + a_t^\kappa. \tag{A20}$$

The two offsets a_n^κ and a_t^κ can easily be expressed from Eqs. (A16) and (A17). Equations (A19) and (A20) or Eqs. (A16) and (A17) are called *transfer equations* [73]. It is easy to show that

$$a_n^\kappa = b_n^\kappa - (1+e_n)\frac{1}{\delta t} u_n^{\kappa-} + \left(\frac{\vec{F}_{\text{ext}}^{\,2_\kappa}}{m_{2_\kappa}} - \frac{\vec{F}_{\text{ext}}^{\,1_\kappa}}{m_{1_\kappa}} \right)\cdot\vec{n}^\kappa, \tag{A21}$$

$$a_t^\kappa = b_t^\kappa - (1+e_t)\frac{1}{\delta t} u_t^{\kappa-} + \left(\frac{\vec{F}_{\text{ext}}^{\,2_\kappa}}{m_{2_\kappa}} - \frac{\vec{F}_{\text{ext}}^{\,1_\kappa}}{m_{1_\kappa}} \right)\cdot\vec{t}^\kappa. \tag{A22}$$

The effect of the approach velocity (left-limit velocity) $(u_n^{\kappa-}, u_t^{\kappa-})$ appears in these equations as an impulse depending on the reduced mass and the restitution coefficient. The effects of contact forces $\vec{f}_i^{\,\lambda}$ acting on the two touching particles i are represented by b_n^κ and b_t^κ, given by

$$b_n^\kappa = \frac{1}{m_{2_\kappa}} \sum_{\lambda(\neq\kappa)} \vec{f}_{2_\kappa}^{\,\lambda}\cdot\vec{n}^\kappa - \frac{1}{m_{1_\kappa}} \sum_{\lambda(\neq\kappa)} \vec{f}_{1_\kappa}^{\,\lambda}\cdot\vec{n}^\kappa, \tag{A23}$$

$$b_t^\kappa = \frac{1}{m_{2_\kappa}} \sum_{\lambda(\neq\kappa)} \vec{f}_{2_\kappa}^{\,\lambda}\cdot\vec{t}^\kappa - \frac{1}{m_{1_\kappa}} \sum_{\lambda(\neq\kappa)} \vec{f}_{1_\kappa}^{\,\lambda}\cdot\vec{t}^\kappa. \tag{A24}$$

The transfer equations (A19) and (A20) define a system of two linear equations between the contact variables at each contact

point. The solution, when the values of a_n and a_t at a contact are assumed, should also verify the contact laws (A2) and (A3). Graphically, this means that the solution is at the intersection between the straight line (A19) and Signorini's graph on the one hand and between Eq. (A20) and Coulomb's graph on the other.

5. Iterative resolution

In order to solve the system of $2N_c$ transfer equations (in 2D) with the corresponding contact law relations, we proceed by an iterative method that converges to the solution simultaneously for all contact forces and velocities. We first consider a single-contact problem that consists of the determination of contact variables f_n^κ, f_t^κ, u_n^κ, and u_t^κ at a single contact given the values of the offsets a_n^κ and a_t^κ at the same contact. The solution is given by intersecting the lines representing transfer equations with Signorini's and Coulomb's graphs. The intersection occurs at a unique point due to the positivity of the coefficients $\mathcal{W}_{k_1k_2}^{\kappa\kappa}$ (positive slope). In other words, the dynamics removes the degeneracy of the contact laws.

Note, however, that the two intersections cannot be established separately when $\mathcal{W}_{nt}^{\kappa\kappa} \neq 0$. To find the local solution, one may consider the intersection of transfer equations with the force axis, i.e., by setting $u_n = u_t = 0$. This yields two values g_n^κ and g_t^κ of f_n^κ and f_t^κ, respectively:

$$g_n^\kappa = \frac{\mathcal{W}_{tt}^{\kappa\kappa} a_n^\kappa - \mathcal{W}_{nt}^{\kappa\kappa} a_t^\kappa}{\mathcal{W}_{nn}^{\kappa\kappa}\mathcal{W}_{tt}^{\kappa\kappa} - \left(\mathcal{W}_{nt}^{\kappa\kappa}\right)^2}, \tag{A25}$$

$$g_t^\kappa = \frac{\mathcal{W}_{nn}^{\kappa\kappa} a_n^\kappa - \mathcal{W}_{tn}^{\kappa\kappa} a_t^\kappa}{\mathcal{W}_{tt}^{\kappa\kappa}\mathcal{W}_{nn}^{\kappa\kappa} - \left(\mathcal{W}_{tn}^{\kappa\kappa}\right)^2}. \tag{A26}$$

It can be shown that the denominator is positive. If $g_n^\kappa < 0$, then the solution is $f_n^\kappa = f_t^\kappa = 0$. This corresponds to a breaking contact. Otherwise, i.e., if $g_n^\kappa \geqslant 0$, we have $f_n^\kappa = g_n^\kappa$. With this value of f_n^κ, we can determine the solution of the Coulomb problem. If $g_t^\kappa > \mu f_n^\kappa$, the solution is $f_t^\kappa = \mu f_n^\kappa$ and in the opposite case, i.e., if $g_t^\kappa < -\mu f_n^\kappa$, the solution is $f_t^\kappa = -\mu f_n^\kappa$ (sliding contact). Otherwise, i.e., when $-\mu f_n^\kappa < g_t^\kappa < \mu f_n^\kappa$, the solution is $f_t^\kappa = g_t^\kappa$ (rolling contact).

In a multicontact system, the terms b_n^κ and b_t^κ in the offsets a_n^κ and a_t^κ depend on the forces and velocities at contacts $\lambda \neq \kappa$[see Eqs. (A21)–(A24)]. Hence the solution for each contact depends on all other contacts of the system and it must be determined simultaneously for all contacts. An intuitive and robust method to solve the system is to search the solution as the limit of a sequence $\{f_n^\kappa(k), f_t^\kappa(k), u_n^\kappa(k), u_t^\kappa(k)\}$ with $\kappa \in [1, N_c]$. Let us assume that the transient set of contact forces $\{f_n^\kappa(k), f_t^\kappa(k)\}$ at the iteration step k is given. From this set, the offsets $\{a_n^\kappa(k), a_t^\kappa(k)\}$ for all contacts can be calculated through relations (A21) and (A22). The local problem can then be solved for each contact κ with these values of the offsets, yielding an updated set of contact forces $\{f_n^\kappa(k+1), f_t^\kappa(k+1)\}$. This correction step is equivalent to the solution of the following local problem:

$$\mathcal{W}_{nn}^{\kappa\kappa} f_n^\kappa(k+1) - \left\{a_n^\kappa(k) - \mathcal{W}_{nt}^{\kappa\kappa} f_t^\kappa(k+1)\right\} \overset{S}{\longleftrightarrow} f_n^\kappa(k+1),$$

$$\mathcal{W}_{tt}^{\kappa\kappa} f_t^\kappa(k+1) - \left\{a_t^\kappa(k) - \mathcal{W}_{nt}^{\kappa\kappa} f_n^\kappa(k+1)\right\} \overset{C}{\longleftrightarrow} f_t^\kappa(k+1).$$

Note that this force update procedure does not require the contact velocities $\{u_n^\kappa(k+1), u_t^\kappa(k+1)\}$ to be calculated as the offsets depend only on the contact forces. The set $\{f_n^\kappa(k), f_t^\kappa(k)\}$ evolves with k by successive corrections and converges to a solution satisfying the transfer equations and contact laws at all potential contacts of the system. The iteration can be stopped when the set $\{f_n^\kappa(k), f_t^\kappa(k)\}$ is stable with regard to the force update procedure within a prescribed precision criterion ε_f:

$$\frac{|f^\kappa(k+1) - f^\kappa(k)|}{f^\kappa(k+1)} < \varepsilon_f \quad \forall\ \kappa. \tag{A27}$$

Finally, from the converged contact forces, the particle velocities $\{\vec{U}^i\}$ can be computed by means of the equations of dynamics (A8).

The iterative procedure depicted above provides a robust method that proves efficient in the context of granular dynamics. The information is treated locally and no large matrices are manipulated during iterations. The number N_i of necessary iterations to converge is strongly dependent on the precision ε_f but not on δt. The number of iterations is substantially reduced when the iteration is initialized with a globally correct guess of the forces. This is the case when the forces at each time step are initialized with the forces computed in the preceding step.

The uniqueness of the solution in a multicontact system with rigid particles is not guaranteed at each step of evolution. We have $3N_p$ equations of dynamics and $2N_c$ contact relations. The unknowns of the problem are $3N_p$ particle velocities and $2N_c$ contact forces. The indeterminacy arises from the fact that the $2N_c$ contact relations are *inequations*. Thus the extent of indeterminacy of the solution reflects all possible combinations of contact forces accommodating those contact relations. The degree of indeterminacy may be high, but it does not imply significant force variability since the solutions are strongly restrained by the contact laws. In practice, the issue is more to find a mechanically admissible solution (verifying the contact laws and equations of dynamics) than indeterminacy. In other words, the variability of the solution is often below the precision controlled by ε_f when the forces are computed at each time step from the forces at the preceding step.

6. Time-stepping scheme

In the CD method, the global problem of the determination of forces and velocities, as described above, is associated with a time-stepping scheme. This scheme is based on the fact that the first condition of Signorini's relations in Eq. (A2) is the only condition referring to space coordinates. Both the equations of dynamics and contact laws are formulated at the velocity level and the first condition of Signorini is accounted for by considering only the *effective contacts* where $\delta_n = 0$. Hence the contact network is defined explicitly from particle positions and it will no longer evolve during the time interval δt. However, the treatment of forces and velocities is fully *implicit* and the right-limit velocities $\{\vec{U}^{i+}, \omega^{i+}\}$ should be used to increment particle positions.

These remarks devise the following time-stepping scheme. Let t and $t + \delta t$ be the considered time interval. The

configuration $\{\vec{r}^i(t)\}$ and particle velocities $\{\vec{U}^i(t),\omega^i(t)\}$ are given at time t. The latter play the role of left-limit velocities $\{\vec{U}^{i-},\omega^{i-}\}$. The contact network $\{\kappa,\vec{n}^\kappa,\vec{t}^\kappa\}$ is set up from the configuration at time t or from an intermediate configuration $\{\vec{r}^i_m\}$ defined by

$$\vec{r}^i_m \equiv \vec{r}^i(t) + \frac{\delta t}{2}\vec{U}^i(t). \tag{A28}$$

When this configuration is used for contact detection, other space-dependent quantities such as the inverse mass parameters $\mathcal{W}^{\kappa\kappa}_{k_1k_2}$ and external forces $\vec{U}^i_{\text{ext}}$ should consistently be defined for the same configuration and at the same time $t+\delta t/2$. Then the forces and velocities are iteratively determined for the contact network and the right-limit particle velocities $\{\vec{U}^{i+},\omega^{i+}\}$ are calculated. The latter correspond to the velocities at the end of the time step $t+\delta t$:

$$\vec{U}^i(t+\delta t) = \vec{U}^{i+}, \tag{A29}$$

$$\omega^i(t+\delta t) = \omega^{i+}. \tag{A30}$$

Finally, the positions are updated by integrating the updated velocities

$$\vec{r}^i(t+\delta t) = \vec{r}^i_m + \frac{\delta t}{2}\vec{U}^i(t+\delta t), \tag{A31}$$

$$\theta^i(t+\delta t) = \theta^i_m + \frac{\delta t}{2}\omega^i(t+\delta t). \tag{A32}$$

This scheme is unconditionally stable due to its inherent implicit time integration. Hence no damping parameters at any level are needed. For this reason, the time step δt can be large. The real limit imposed on the time step is cumulative roundoff errors in particle positions since the latter are updated from the integration of the velocities. Although the excessive overlaps have no dynamic effect in the CD method, they falsify the geometry and thus the evolution of the system. A sufficiently high precision or a large enough number of iterations is required to avoid such errors. The time step is not a precision parameter but a coarse-graining parameter for nonsmooth dynamics. It should be reduced if the impulse dynamics at small time scales is of interest.

[1] K. Mair, K. M. Frye, and C. Marone, J. Geophys. Res. **107**, 2219 (2002).
[2] F. Alonso-Marroquin and H. J. Herrmann, Phys. Rev. E **66**, 021301 (2002).
[3] A. Mirghasemi, L. Rothenburg, and E. Maryas, Geotechnique **52**, 209 (2002).
[4] C. Nouguier-Lehon, B. Cambou, and E. Vincens, Int. J. Numer. Anal. Meth. Geomech. **27**, 1207 (2003).
[5] Y. Guo and J. Morgan, J. Geophys. Res. **109**, 12305 (2004).
[6] J. L. Anthony and C. Marone, J. Geophys. Res. **110**, B08409 (2005).
[7] A. Pena, A. Lizcano, F. Alonso-Marroquin, and H. Herrman, Int. J. Numer. Anal. Meth. Geomech. **1145**, 1 (2006).
[8] E. Azéma, F. Radjai, R. Peyroux, and G. Saussine, Phys. Rev. E **76**, 011301 (2007).
[9] S. A. Galindo-Torres, J. D. Munoz, and F. Alonso-Marroquin, Phys. Rev. E **82**, 056713 (2010).
[10] E. Azéma, F. Radjaï, and G. Saussine, Mech. Mater. **41**, 729 (2009).
[11] E. Azéma, F. Radjai, R. Peyroux, F. Dubois, and G. Saussine, Phys. Rev. E **74**, 031302 (2006).
[12] E. Azéma, Y. Descantes, N. Roquet, J.-N. Roux, and F. Chevoir, Phys. Rev. E **86**, 031303 (2012).
[13] A. Donev, F. H. Stillinger, P. M. Chaikin, and S. Torquato, Phys. Rev. Lett. **92**, 255506 (2004).
[14] S. Sacanna, L. Rossi, A. Wouterse, and A. P. Philipse, J. Phys.: Condens. Matter **19**, 376108 (2007).
[15] I. Zuriguel, T. Mullin, and J. M. Rotter, Phys. Rev. Lett. **98**, 028001 (2007).
[16] I. Zuriguel and T. Mullin, Proc. R. Soc. A **464**, 99 (2008).
[17] R. C. Hidalgo, I. Zuriguel, D. Maza, and I. Pagonabarraga, Phys. Rev. Lett. **103**, 118001 (2009).
[18] E. Azéma and F. Radjaï, Phys. Rev. E **81**, 051304 (2010).
[19] T. Kanzaki, M. Acevedo, I. Zuriguel, I. Pagonabarraga, D. Maza, and R. Hidalgo, Eur. Phys. J. E **34**, 133 (2011).
[20] E. Azéma and F. Radjai, Phys. Rev. E **85**, 031303 (2012).
[21] B. Saint-Cyr, C. Voivret, J. Delenne, F. Radjai, and P. Sornay, in *Powders and Grains 2009*, in *Proceedings of the Sixth International Conference on Micromechanics of Granular Media*, AIP Conf. Proc. No. 1145 (AIP, New York, 2009), pp. 389–392.
[22] B. Saint-Cyr, J.-Y. Delenne, C. Voivret, F. Radjai, and P. Sornay, Phys. Rev. E **84**, 041302 (2011).
[23] G. Saussine, C. Cholet, P. Gautier, F. Dubois, C. Bohatier, and J. Moreau, Comput. Methods Appl. Mech. Eng. **195**, 2841 (2006).
[24] E. Nezami, Y. Hashash, D. Zaho, and J. Ghaboussi, Int. J. Numer. Anal. Meth. Geomech. **30**, 783 (2006).
[25] *Discrete Numerical Modeling of Granular Materials*, edited by F. Radjai and F. Dubois (Wiley-ISTE, New-York, 2011).
[26] E. Azéma, F. Radjai, R. Peyroux, V. Richefeu, and G. Saussine, Eur. Phys. J. E **26**, 327 (2008).
[27] J. J. Moreau, J. Diff. Equ. **26**, 347 (1977).
[28] J. J. Moreau, C. R. Acad. Sci. Paris, Série II **296**, 1473 (1983).
[29] J. J. Moreau, in *Topics in Nonsmooth Mechanics*, edited by P. Panagiotopoulos and G. Strang (Bikhäuser, Basel, 1988), pp. 1–74.
[30] J. J. Moreau, in *Nonsmooth Mechanics and Applications*, edited by J. J. Moreau and P. Panagiotopoulos, CISM Vol. 302 (Springer, Wien, 1988), pp. 1–82.
[31] J. J. Moreau, in *Powders & Grains 93* (Balkema, Rotterdam, 1993), p. 227.
[32] J.-J. Moreau, Eur. J. Mech. A Solids **13**, 93 (1994).
[33] M. Jean and E. Pratt, Int. J. Eng. Sci. **23**, 497 (1985).
[34] M. Jean, Arch. Mech. Warszawa **40**, 677 (1988).
[35] M. Jean and J. J. Moreau, in *Proceedings of Contact Mechanics International Symposium*, edited by A. Curnier (Presses Polytechniques et Universitaires Romandes, Lausanne, 1992), pp. 31–48.

[36] M. Jean, F. Jourdan, and B. Tathi, in *Handbooks on Theory and Engineering Applications of Computational Methods*, edited by M. J. M. Barata Marques, in *Proceedings of the IDDRG 1994 Open Sessions of the 18th Biennial Congress* (IDDRG, Lisboa, 1994).
[37] M. Jean, *Frictional Contact in Rigid or Deformable Bodies: Numerical Simulation of Geomaterials* (Elsevier Science, Amsterdam, 1995), pp. 463–486.
[38] M. Jean, Comput. Methods Appl. Mech. Eng. **177**, 235 (1999).
[39] P. Cundall, in *Proceedings of the Symposium of the International Society of Rock Mechanics, Nancy, France, 1971*, Vol. 1 (ISRM, Lisboa, 1971), pp. 132–150.
[40] P. A. Cundall and O. Strack, Geotechnique **29**, 47 (1979).
[41] C. Thornton and K. K. Yin, Powder Technol. **65**, 153 (1991).
[42] H. J. Herrmann, Molecular dynamics simulations of dry granular media, in The first Nisshin Engineering Particle Technology International Seminar: Discrete Particle Simulations in Powder Technology, Osaka, Japan, 1993, p. 8.
[43] C. Thornton, Computer simulation of impact fracture/fragmentation, in The first Nisshin Engineering Particle Technology International Seminar: Discrete Particle Simulations in Powder Technology, Osaka, Japan, 1993, p. 17.
[44] T. Pöschel and V. Buchholtz, J. Phys. I (Paris) **5**, 1431 (1995).
[45] C. Thornton, J. Appl. Mech. **64**, 383 (1997).
[46] S. Luding, in *Physics of Dry Granular Media,* edited by H. J. Herrmann, J.-P. Hovi, and S. Luding, NATO Advanced Studies Institute, Series E: Applied Science, Vol. 350 (Kluwer Academic, Dordrecht, 1998), p. 285.
[47] S. McNamara and H. Herrmann, Phys. Rev. E **70**, 061303 (2004).
[48] X. Garcia and E. Medina, Phys. Rev. E **75**, 061308 (2007).
[49] F. A. Gilabert, J.-N. Roux, and A. Castellanos, Phys. Rev. E **75**, 011303 (2007).
[50] V. Richefeu, M. S. El Youssoufi, R. Peyroux, and F. Radjai, Int. J. Numer. Anal. Methods Geomech. **32**, 1365 (2007).
[51] V. Visseq, A. Martin, D. Iceta, E. Azéma, D. Dureisseix, and P. Alart, Comput. Mech. **49**, 709 (2012).
[52] H.-G. Matuttis, S. Luding, and H. J. Herrmann, Powder Technol. **109**, 278 (2000).
[53] F. Dubois and M. Jean, in *Analysis and Simulation of Contact Problems*, edited by P. Wriggers and U. Nackenhorst, Lecture Notes in Applied and Computational Mechanics, Vol. 27 (Springer, Berlin, 2006), pp. 375–378.
[54] A. Taboada, K. J. Chang, F. Radjai, and F. Bouchette, J. Geophys. Res. **110**, 1 (2005).
[55] C. Voivret, F. Radjai, J.-Y. Delenne, and M. S. El Youssoufi, Phys. Rev. E **76**, 021301 (2007).
[56] GDR-MiDi, Eur. Phys. J. E **14**, 341 (2004).
[57] J. Mitchell and K. Soga, *Fundamentals of Soil Behavior* (Wiley, New York, 2005).
[58] www.cgp-gateway.org/ref016.
[59] J. J. Moreau, in *Friction, Arching, Contact Dynamics*, edited by D. E. Wolf and P. Grassberger (World Scientific, Singapore, 1997), pp. 233–247.
[60] M. Oda, J. Koshini, and S. Nemat-Nasser, Geotechnique **30**, 479 (1980).
[61] L. Rothenburg and R. J. Bathurst, Geotechnique **39**, 601 (1989).
[62] F. Radjai, D. E. Wolf, M. Jean, and J. J. Moreau, Phys. Rev. Lett. **80**, 61 (1998).
[63] F. Radjai, H. Troadec, and S. Roux, in *Granular Materials: Fundamentals and Applications*, edited by S. Antony, W. Hoyle, and Y. Ding (Royal Society of Chemistry, Cambridge, 2004), pp. 157–184.
[64] B. Cambou, P. Dubujet, and C. Nouguier-Lehon, Mech. Mater. **36**, 1185 (2004).
[65] C. Nouguier-Lebon, E. Vincens, and B. Cambou, Int. J. Solids Struct. **42**, 6356 (2005).
[66] N. Estrada, A. Taboada, and F. Radjai, Phys. Rev. E **78**, 021301 (2008).
[67] C. Voivret, F. Radjai, J.-Y. Delenne, and M. S. El Youssoufi, Phys. Rev. Lett. **102**, 178001 (2009).
[68] N. Estrada, E. Azéma, F. Radjai, and A. Taboada, Phys. Rev. E **84**, 011306 (2011).
[69] F. Radjai, J.-Y. Delenne, E. Azéma, and S. Roux, Granular Matter **14**, 259 (2012).
[70] H. Ouadfel and L. Rothenburg, Mech. Mater. **33**, 201 (2001).
[71] F. Radjaï and V. Richefeu, Mech. Mater. **41**, 715 (2009).
[72] J. Moreau, in *Novel Approaches in Civil Engineering*, edited by M. Frémond and F. Maceri, Lecture Notes in Applied and Computational Mechanics, Vol. 14 (Springer-Verlag, Berlin, 2004), pp. 1–46.
[73] F. Radjaï and E. Azéma, Eur. J. Env. Civil Eng. **13**, 203 (2009).